## PAPER

Check for updates

# Durable Zn-ion hybrid capacitors using 3D printed carbon composites†

Goli Nagaraju, ‡ Stefano Tagliaferri, ‡ Apostolos Panagiotopoulos, Mauro Och, Rachael Quintin-Baxendale and Cecilia Mattevi *

Rechargeable Zn-ion hybrid capacitors (ZHCs) have gained considerable attention towards future energy storage applications owing to their non-flammable nature, high abundance of raw materials and remarkable energy storage performance. However, the uncontrolled growth of dendrites, interfacial corrosion of Zn anodes and limited mass loading of cathode materials, hinders their practical applicability. Herein, we demonstrate ZHCs with enhanced capacity and durability using a synergistic combination of a hybrid-ion electrolyte and a high-mass loading three-dimensionally (3D) printed graphene–carbon nanotube (Gr–C) cathode. The hybrid electrolyte composed of NaCl and ZnSO$_4$, features higher ionic conductivity and lower pH compared with pristine ZnSO$_4$, which enable uniform plating/stripping of Zn$^{2+}$ ions on Zn anode, as demonstrated by *in situ* electrochemical and *ex situ* ToF-SIMs characterizations. Additionally, the multi-layered 3D Gr–C composite electrodes in ZHCs enable higher energy storage performance due to their porous architectures, high ion accessibility and dual-ion charge storage contributions. As a result, the 3D Gr–C//Zn cell unveiled a maximum capacity of 0.84 mA h cm$^{-2}$ at 3 mA cm$^{-2}$ with a high life cycle (78.7% at 20 mA cm$^{-2}$) compared to the pristine electrolyte-based ZHCs (0.72 mA h cm$^{-2}$ and 14.8%). The rapid rate measurements that we propose along with benchmarked energy density (0.87 mW h cm$^{-2}$) and power density (31.7 mW cm$^{-2}$) of hybrid electrolyte-based 3D Gr–C//Zn, pave the way for the development of dendrite-free and highly durable 3D energy storage devices.

## 1. Introduction

The expanding market of self-powered portable devices requires new energy storage systems that are inherently safe, small, and efficient. Due to their high energy density and large operating potential, lithium-ion batteries (LIBs) are currently used in portable electronics.[1–4] However, LIBs normally rely on flammable materials and hazardous organic electrolytes which pose safety concerns.[5] As for wearable and portable devices, the energy requirements are generally limited to ~1–1000 mW h, thus metal-ion hybrid capacitors based on aqueous electrolytes could achieve energy densities adequate to power these devices.[6–8] With a combination of capacitive- and battery-like materials, aqueous metal-ion capacitors represent a cheaper and safer alternative to LIBs. Specifically, zinc-ion hybrid capacitors (ZHCs) have attracted promising interest owing to the intrinsic safety, low cost, and natural abundance of the raw materials.[9,10] In ZHCs, zinc (Zn) metal can be directly employed

as the battery-type anode, since it has a low reduction potential of −0.76 V *vs.* SHE and a high overpotential for hydrogen evolution, which allow the stripping and the plating of Zn$^{2+}$ ions in water electrolytes.[11,12] Despite presenting a high gravimetric capacity of 820 mA h g$^{-1}$, Zn metal anodes suffer from poor rate capability and short life cycling due to dendrite growth, corrosion processes and irreversible side reactions which lead to the formation of inert by-products.[13–15]

Recently, different approaches have been proposed to alleviate such issues, including the structural redesign of the electrode geometry and the modification of both the electrode surface and electrolyte composition to promote reversible charge storage reactions.[16–19] Notably, Zeng *et al.*[17] have proposed the construction of Zn anodes on CNT-covered carbon cloth, which led to a reduced local current density inside the electrode. This approach resulted in a more uniform electric field in the proximity of the electrode surface, a reduced voltage hysteresis for Zn plating and diminished dendrite growth, respectively. In contrast, Guo *et al.*[20] have modified the surface of Zn anodes *via* the deposition of a tin (Sn) layer. The Sn coating was found to suppress the corrosion of Zn and to prevent the formation of dendrites in ZnSO$_4$ electrolyte. A similar effect was obtained by sputtering gold nanoparticles on Zn foils, which has improved the cycling stability and ultimately

*Department of Materials, Imperial College London, London SW7 2AZ, UK. E-mail: c. mattevi@imperial.ac.uk; Tel: +44 (0)2075940833*

† Electronic supplementary information (ESI) available. See https://doi.org/10.1039/d2ta03488c

‡ G. N. and S. T. equally contributed to this work.

This journal is © The Royal Society of Chemistry 2022

*J. Mater. Chem. A*, 2022, **10**, 15665–15676 | **15665**

the lifetime of the device.[21] Although these efforts have allowed to increase of the life cycling and reversibility of the Zn anodes, surface modifications often rely on toxic and expensive chemicals, and increasing surface area of the Zn anodes worsens the spontaneous corrosion of Zn in aqueous electrolytes. Additionally, both approaches propose a multistep preparation procedure for the Zn anode, which is time consuming, and increases the costs of ZHCs. Another approach to extend the lifetime of Zn anodes is focused on the electrolyte. By altering the electrolyte composition, it is been possible to prevent irreversible side reactions, including hydrogen evolution reaction (HER) and passivation.[19,22,23] Additives such as LiCl and $Na_2SO_4$ can inhibit the growth of nonconductive by-products like zinc hydrosulphates[22] while enhancing the ionic conductivity of the electrolyte. It has been demonstrated that the addition of LiCl can promote the formation of a protective oxide layer on the Zn anode and also reduce the pH of $ZnSO_4$ electrolytes, ultimately hindering the growth of nonconductive hydroxysulfates.[22] This technique can be easily implemented in the manufacturing process of ZHCs and does not require costly and hazardous reagents, representing a promising strategy to enhance the stability of aqueous energy storage devices.

The choice of a stable, high-energy density cathode material is key for the development of durable and efficient ZHCs. Zn metal anodes are often coupled with carbon-based cathodes, which act as capacitive electrodes, storing charges through electric double layer or pseudocapacitive processes.[24–26] Common carbon cathodes include activated carbon and reduced graphene oxide, which can achieve excellent power densities, higher than 10 mW $cm^{-2}$, and stable cycling performance for thousands of consecutive charge–discharge cycles.[26,27] MXenes have also been widely investigated as ZHC cathodes for their ability to store electrical charge *via* faradaic pseudocapacitive mechanisms, leading to energy densities of $\sim$0.1 mW h $cm^{-2}$.[28] The energy density of ZHCs cathode can be further improved through three-dimensional (3D) electrodes, which provides ultra-high areal loading of active material over small footprint areas and minimize the weight fraction of inactive components, *i.e.* current collector, separator and packaging. However, the 3D design of the cathode structure must be precisely controlled to simultaneously ensure good electrolyte penetration, fast charge transport and high mass loading. Increasing the thickness of the cathode without tailoring the electrode geometry may be detrimental to the rate performance and power density, since the pathways for charge transport would be significantly lengthened.[29,30]

In this work, we demonstrate a ZHC with maximum areal capacity of 0.84 mA h $cm^{-2}$ at 3 mA $cm^{-2}$ and with a life cycle retention of 78.7% at a high current density of 20 mA $cm^{-2}$ *via* a dual approach consisting in fabricating electrodes with high mass loading and employing a new hybrid electrolyte. We have used 3D printing robocasting to fabricate graphene–carbon nanotubes (Gr–C) cathodes for ZHCs, which uniquely allowed to fine tune the Gr–C electrode architectures to promote the penetration of the aqueous electrolyte and to shorten the ionic transport distances. Additionally, 3D printing allowed us to achieve high mass loading cathodes within small footprint areas. Furthermore, we demonstrated here dendrite-free $Zn^{2+}$ ion plating/stripping, increased energy density and enhanced cycling life of the Zn metal anode, using a hybrid-electrolyte based on $ZnSO_4$ with the inclusion of NaCl. NaCl served as a new, cost-effective pH modifier preventing the formation of dendrites and corrosion by-products. The rate performance of the high-mass loading cathodes in 3D Gr–C//Zn cells were further assessed using a simple chronoamperometric (CA) technique, which allows the collection of many rate data points within a short time. Rate performance data are usually obtained through galvanostatic charge and discharge (GCD) tests at different current densities, depending on the mass loading of the active material. Although the charge–discharge process in thin-film devices is typically fast, the larger charge-storage capability of hybrid ZHCs with 3D electrodes leads to long charge–discharge times, resulting in time consuming GCD tests. Accordingly, we propose the use of a fast CA test as a reliable and fast alternative to conventional GCD analysis to characterize the rate performance of high-mass loading 3D Gr–C//Zn-based ZHCs.

## 2. Results and discussion

The aqueous Gr–C composite inks were formulated by adding pristine Gr platelets and sodium carboxymethyl cellulose (CMC) to an aqueous dispersion of single walled carbon nanotubes (CNTs). The materials were then mixed at high shear, until a homogenous slurry was obtained. CMC acts as an effective thickening agent for the aqueous ink, increasing the viscosity of the suspension and promoting the dispersion of Gr and carbon nanotubes. While carbon nanotubes are known to enhance the connectivity of the network of Gr platelets,[31] endowing the ink with rheological features suitable for printing and improving the mechanical strength and electrical properties of the final electrodes. The ink formulation process did not alter the properties of Gr platelets and CNTs, as demonstrated by XRD, XPS and Raman spectroscopy (Fig. S1†), which show the characteristic features of pristine Gr platelets and single walled carbon nanotubes (as detailed in the ESI†). The ink should satisfy specific rheological properties to be printable and to enable mechanically stable 3D architecture of arbitrary geometry. Firstly, the ink should flow continuously with a shear-thinning behaviour during printing. Secondly, a printed filament should be able to support the weight of the subsequently printed layers on top, to form a self-standing architecture (solid behaviour at rest). The yield stress of the ink, *i.e.*, the threshold value of stress that marks the transition between the solid- and fluid-like regime, was measured *via* oscillatory tests, recording the viscoelastic response of the sample at increasing oscillatory stress (Fig. 1a). At an oscillation stress of $\sim$50 Pa, the ink transitions from a linear viscoelastic response to a non-linear response, with the onset of irreversible modification in the ink microstructure. When the yield stress ($\sim$435 Pa) is reached, the inner structure of the ink is destroyed by the oscillatory shear and the ink exhibit liquid-like flow properties, with the loss modulus prevailing over the storage modulus. The viscoelastic response in the linear region (below $\sim$50 Pa) was further

15666 | *J. Mater. Chem. A*, 2022, **10**, 15665–15676

This journal is © The Royal Society of Chemistry 2022

characterized *via* frequency sweep tests (Fig. 1b), indicating a solid-like, elastic behaviour in the interval of frequencies investigated, which allows the structure to retain its shape at rest. The high rest storage modulus $\sim 1.5 \times 10^5$ Pa minimizes the bending of overhanging filaments after extrusion, ensuring shape preservation during the drying process. Additionally, during shear flow the ink exhibits a marked shear-thinning behaviour (Fig. 1c), with a flow index $\sim 0.24$ and a notable reduction of viscosity (from $\sim 10^5$ to $\sim 10$ Pa s) in the range of shear rates investigated. In the absence of CNTs, the storage modulus of the ink decreases to $\sim 5 \times 10^4$ Pa (Fig. S2†), resulting in more compliant ink filaments that can bend and buckle after deposition. This highlights the importance of CNTs in enhancing the connectivity of the network and improving the printability of the composite ink. The high shear-thinning flow during extrusion, combined with the large rest storage modulus and yield stress, allowed the fabrication of 3D printed woodpile electrodes with exceptional thickness (up to $\sim 3.1$ mm, Fig. S4a and b†), which presented no mechanical instabilities after drying in air (Fig. 1d and f). The volume and areal loading of active material could be finely controlled *via* the layer-by-layer deposition process (Fig. 1g), reaching a loading $\sim 20$ times higher than thin film electrodes for the 12-layer structures. Despite the large mass loading, the electrodes still possess a large electroactive area in contact with the electrolyte, owing to their tailored architecture of periodic channels and large pores between the printed filaments, which promote the infiltration of the electrolyte. As elucidated by SEM and TEM imaging (Fig. 1e and S1d–f†), CNTs cover the surface of the Gr platelets, bridging neighbouring platelets and thus enhancing electron transport in the 3D structure. As a result, the electrical conductivity of the Gr–C structure is superior to the bare Gr electrodes by a factor of two ($\sim 8.64$ S cm$^{-1}$). The electrical conductivity of the printed electrodes can be increased up to $\sim 36.97$ S cm$^{-1}$ and the stability of the electrodes in aqueous electrolytes can be enhanced through a thermal annealing at 350 °C in inert atmosphere (Fig. 1i and S4d†). At this temperature, the inert cellulose binder pyrolyzes, as indicated by the TGA/DTA analysis in Fig. 1h, leaving a robust 3D structure made of Gr platelets interconnected by conductive CNTs. On the contrary, the network-like Gr–C architecture was not observed when the CNTs powder was directly mixed with Gr platelets ink, which resulted in aggregated CNTs chunks between the Gr platelets (Fig. S3†). Therefore, the aqueous dispersion of CNTs is desirable to obtain highly conductive and interconnected 3D electrodes.

To extend the cycling life of ZHC, we developed a cost-effective hybrid NaCl + ZnSO$_4$ electrolyte and compared its feasibility with a conventional 2 M ZnSO$_4$ electrolyte. The addition of NaCl to the ZnSO$_4$ electrolyte effectively increases the ionic conductivity (Fig. S5a†) and significantly reduces the pH of the solution from 6.4 to 3.7 (as measured for the uncycled electrolyte, Fig. 2c). This could be ascribed to the increased polarization of the O–H bonds in zinc-coordinated water molecules and to the improved stabilization of zinc hydroxide $[\text{Zn(OH}_2)_x\text{OH}]^+$ with respect to Zn–water complexes.[22,32] In fact, Zn$^{2+}$ ions can form octahedral complexes with water molecules

that act as Lewis-acid assisted Brønsted acids, releasing hydrogen cations from the solvation shell of Zn$^{2+}$.[33,34] The lower pH is less favourable to the formation of zinc hydroxysulphate corrosion by-products, which are commonly observed in pristine ZnSO$_4$ electrolytes, forming an insulating deposit on the anode surface. Additionally, the chloride (Cl$^-$) anions of the hybrid electrolyte are known to have an aggressive and de-passivating effect on Zn, inhibiting the formation of insulating corrosion layers and thus contributing to the preservation of a bare Zn anode surface.[35,36] The benefit of the NaCl additive in extending the cycling stability of Zn anodes were demonstrated through chronopotentiometry (CP) charge–discharge tests (Fig. 2a and b). Pristine ZnSO$_4$ and hybrid electrolyte symmetric pouch cells consisting of two identical Zn metal electrodes ($1 \times 1$ cm$^2$) and a glass-fibre separator were charged and discharged to a capacity of 0.25 mA h cm$^{-2}$ with a current density of 0.5 mA cm$^{-2}$ (Fig. 2a). Both devices display electrochemical stability, with minimal variations in the plating and stripping potential up to 450 h. However, the hybrid electrolyte leads to a much lower deposition overpotential (initial potentials of $\sim 21$ mV *vs.* $\sim 48$ mV and final potentials of $\sim 20$ mV *vs.* $\sim 52$ mV, respectively) owing to its higher ionic conductivity (Fig. S5a†). The difference between the two electrolytes was further investigated by increasing the deposition capacity to 5 mA h cm$^{-2}$ (at a current density of 10 mA cm$^{-2}$, Fig. 2b). The deposition overpotential for the bare ZnSO$_4$ cell starts to rapidly increase after $\sim 80$ h, spiking to over 500 mV after 85 h. This is due to the formation of passivation products on the surface of the Zn electrodes, as indicated by the visual inspection of the electrodes after cycling. Indeed, the change in colour of the cycled Zn suggests that the hybrid-electrolyte anodes have a similar surface morphology to the blank Zn foil (Fig. S5b†), while the ones cycled in the pristine ZnSO$_4$ electrolyte present an extra coating layer (Fig. 2f). Thus, the hybrid electrolyte retains a small deposition overpotential ($\sim 27$ mV final deposition potential *vs.* $\sim 37$ mV initial deposition potential) for more than 450 h, by the virtue of a higher interfacial conductivity. The observed minor variations can be ascribed to temperature changes during the prolonged cycling test. The exchange current measured *via* linear sweep voltammetry for the hybrid electrolyte and the pristine electrolyte are similar, suggesting that no major onset of hydrogen evolution has occurred despite the more acidic pH (Fig. 2d and Table S1†). The different cycling behaviour of Zn metal (after plating–stripping tests) in the two electrolytic systems was further investigated *via ex situ* SEM and optical microscope analysis, as presented in Fig. 2i and j and S5c.† The Zn electrodes cycled in the pristine electrolyte exhibit a thick layer of insulating by-products/dead Zn in the form of lumps and large vertical hexagonal platelets. On the contrary, the Zn electrodes cycled in the hybrid electrolyte exhibit a flat foil like appearance with small and isolated particles on the top of the Zn foil surface. The ToF-SIMS mapping in Fig. 2k and S6† indicates that the surface of the electrodes cycled in pristine ZnSO$_4$ is completely coated by oxygen- and sulphur-containing species. These were identified as zinc oxide (ZnO) and zinc hydrosulphate tetrahydrate (Zn$_4$SO$_4$(OH)$_6\cdot$4H$_2$O, JCPDS #044-0673) *via ex situ* XRD analysis (Fig. 2e). On the electrodes cycled

This journal is © The Royal Society of Chemistry 2022

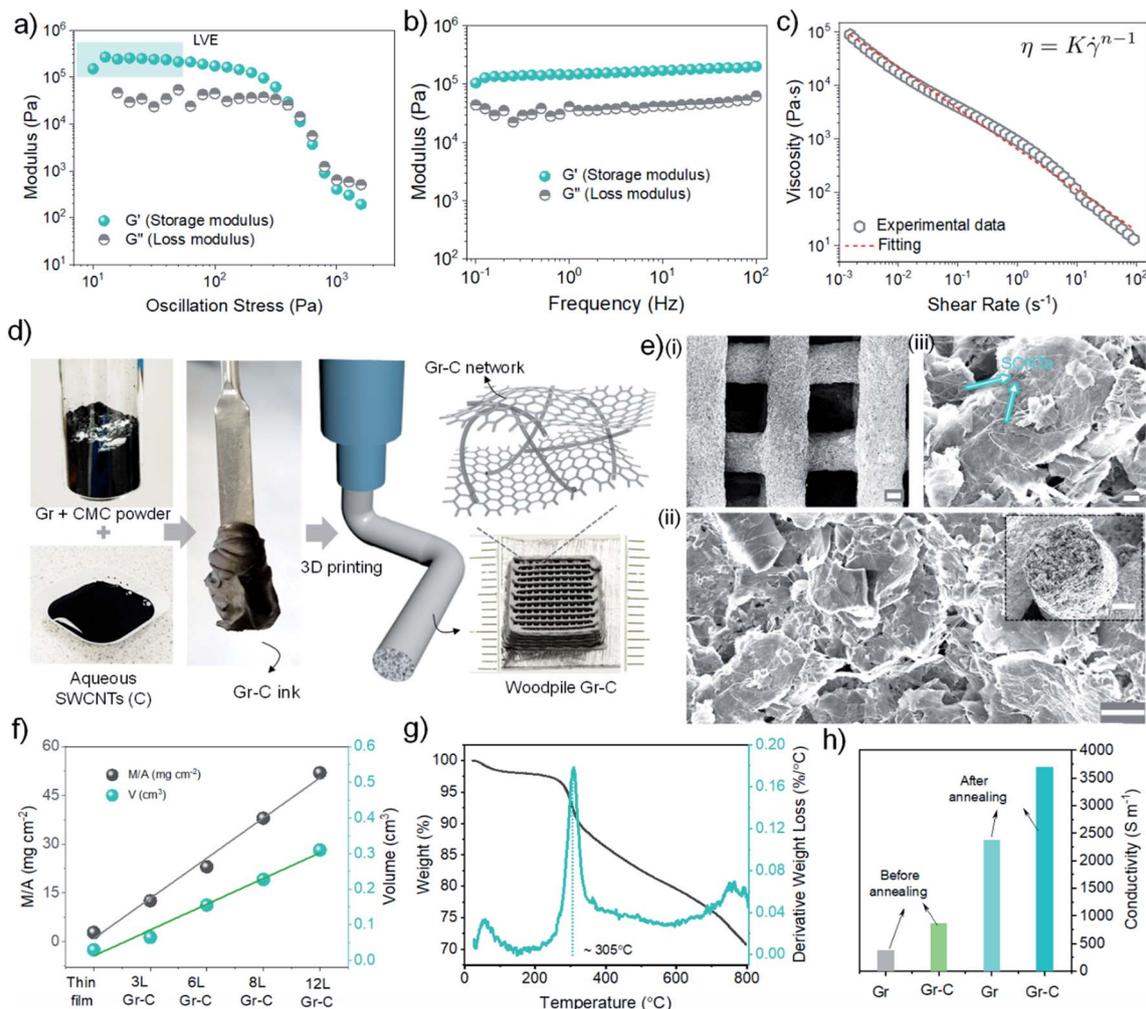*J. Mater. Chem. A*, 2022, **10**, 15665–15676 | **15667**

**Fig. 1** Rheological properties and characterisation of the Gr−C composite/3D structures. (a) Storage modulus and loss modulus of the Gr−C ink with respect to oscillation stress, (b) frequency sweep measurement of Gr−C ink, analysed in the linear viscoelastic region and (c) apparent viscosity as a function of shear rate for the Gr−C ink. (d) Digital photographs of Gr platelets powder, aqueous dispersion of SWCNTs, Gr−C ink and the schematic illustration of the 3D printing process of network-like GrC composite structures. (e) Low- and high-magnification SEM images (scale bars: (i) 100 μm, (ii) 5 μm, (iii) 1 μm, respectively) of 3D printed woodpile Gr−C structure, showing the Gr platelets were interconnected with bundles of SWCNTs. The inset of (e) (ii) shows the cross-sectional SEM image of a printed Gr−C strut (scale bar: 100 μm). (f) Areal mass loading (mg cm$^{-2}$) and volume (cm$^3$) of thin-film/3D printed Gr−C electrodes, showing the linear increment of corresponding values upon increasing the number of printed layers (3−12L). (g) Thermogravimetric analysis (TGA) and differential thermal analysis (DTA) of Gr−C composite as a function of the heating temperature. (h) Conductivity values of thin-film Gr- and Gr−C electrodes before and after heat treatment.

in the hybrid electrolyte, sulphur and oxygen are instead predominantly concentrated in the small hexagonal platelets observed in the SEM images (Fig. 2j), which also contain chlorine. In this case, XRD analysis revealed that the dispersed platelets consist of sodium gordaite crystals (NaZn$_4$(SO$_4$)Cl(OH)$_6$·6H$_2$O, JCPDS #050-1579), made of stacked hydroxide layers separated by intermediate water molecules and ions (Na$^+$ and Cl$^-$).[37] The effects of these different corrosion by-products on the charge transfer kinetic were investigated using *in situ* electrochemical impedance spectroscopy (EIS) measurements recorded after consecutive stripping/plating cycles of Zn//Zn cells (Fig. 2g and h and S5d†). The real intercept of impedance for the hybrid electrolyte cell is significantly lower than the pristine ZnSO$_4$ electrolyte (∼1.61 Ω *vs.* ∼7.86 Ω), as expected

from ionic conductivity characterisation. Two depressed semicircles, resulting from the interfacial impedance at the Zn/electrolyte and Zn/passivated layer boundary, are clearly visible in the Nyquist plot of the hybrid electrolyte. The decrease in diameter over cycling because of the reduced transport resistance and surface roughening of the electrodes in the more acidic electrolyte.[38,39] On the contrary, the depressed semicircles in the pristine electrolyte remain constant in size, and present a very high value of overall impedance of ∼103 Ω (*vs.* 33 Ω for the hybrid electrolyte after 25 cycles at 1 Hz). Coulombic efficiency (CE) of Zn//Cu cells using pristine and hybrid electrolytes was also measured at different charges, ranging from 1 to 10 mA cm$^{-2}$, as presented in Fig. S7.†
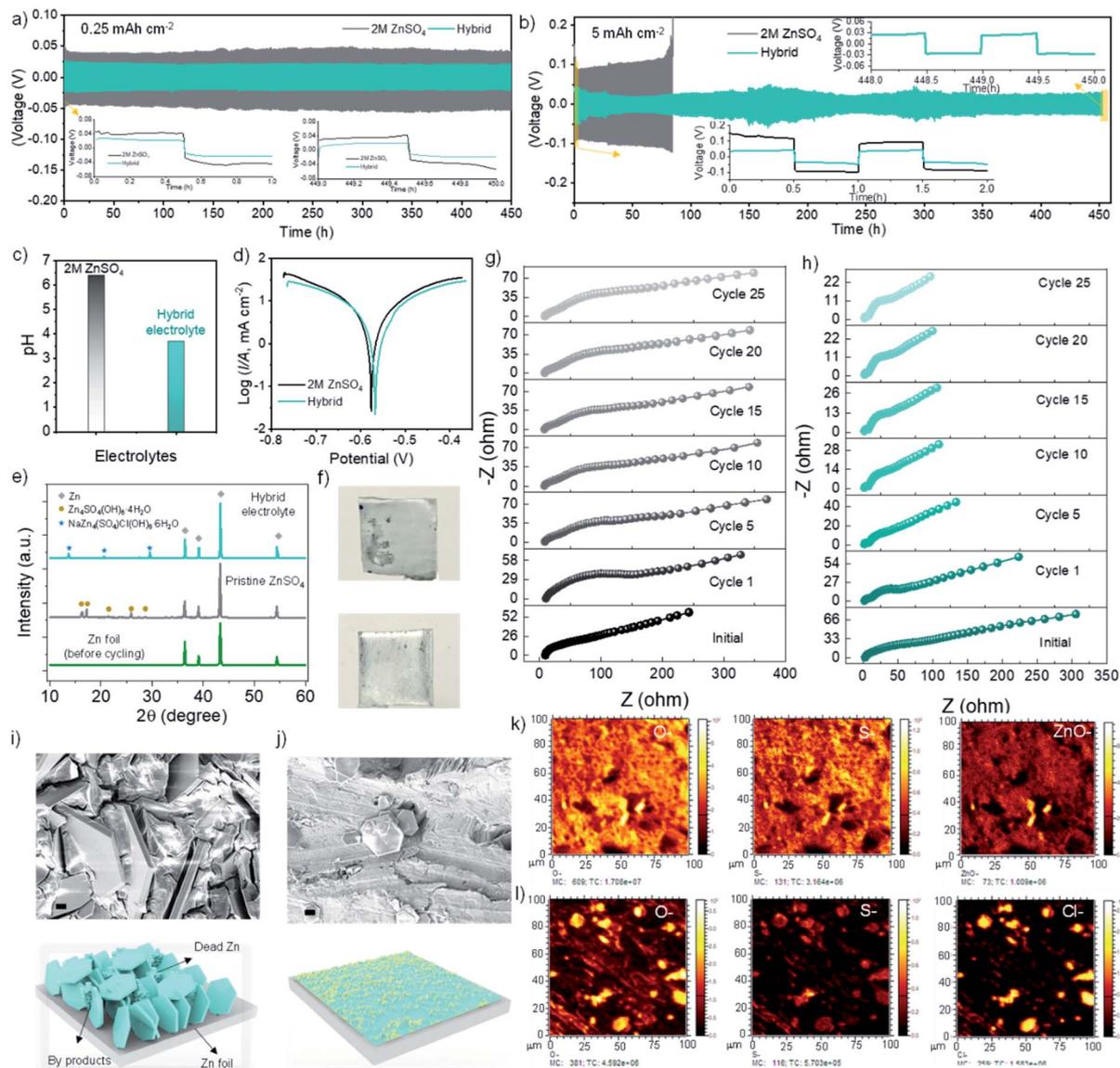
**15668** | *J. Mater. Chem. A*, 2022, **10**, 15665–15676

This journal is © The Royal Society of Chemistry 2022

**Fig. 2** Electrochemical performance and characterisation of symmetric cells based on Zn metal with pristine 2 M ZnSO$_4$ and hybrid electrolyte (2 M ZnSO$_4$ + NaCl). (a) Plating/stripping voltage *vs.* time profiles of Zn//Zn symmetric cells measured at low capacity of 0.25 mA h cm$^{-2}$ and (b) high capacities of 5 mA h cm$^{-2}$ using pristine ZnSO$_4$ and hybrid electrolytes. (c) pH values and (d) exchange current densities of pristine ZnSO$_4$ and hybrid electrolyte measured with Tafel plots (collected at the scanning rate of 1 mV s$^{-1}$). (e) *Ex situ* XRD plots and (f) digital photographs of Zn anodes after cycling in pristine ZnSO$_4$ (top) and hybrid electrolyte (bottom) after 450 h. *In situ* Nyquist plots of Zn//Zn symmetric cells measured using (g) pristine ZnSO$_4$ and (h) hybrid electrolyte, respectively. These plots were obtained after each stripping/plating cycle of Zn//Zn symmetric cell in the corresponding electrolytes. (i and j) *Ex situ* SEM images (scale bar: 2 μm) with schematic illustrations and (k and l) *ex situ* ToF-SIMs mapping images of cycled Zn metal using pristine ZnSO$_4$ and hybrid electrolyte.

The feasibility of the hybrid electrolyte and 3D printed Gr–C electrodes was evaluated by assembling a full cell (3D Gr–C//Zn) Zn-ion hybrid capacitor (ZHC). The ZHC cell was fabricated using 3D Gr–C (6 layers) as cathode, Zn metal as anode and a glass-fibre filter paper as separator with few mL of the hybrid electrolyte (2 M ZnSO$_4$ + NaCl), as presented in the photographs and schematic illustration in Fig. 3a(i–iii). The addition of NaCl into the ZnSO$_4$ electrolyte enables versatile features in terms of energy storage and durability. The hybrid electrolyte prevents the deposition of side-products on the Zn anodic side during the electrochemical processes, owing to two factors. The former is the polarizing behaviour of Cl$^-$ ions, which enable to maintain a slightly acidic environment in the cell, while the Na$^+$ cations provide an electrostatic shield effect on the Zn anode, which allows the uniform plating/stripping of Zn and prevents the mass growth of Zn dendrites.[22,32,40] The Na$^+$ cations present a reduction potential significantly lower than Zn$^{2+}$, therefore they can be adsorbed on the anode surface, providing an electrostatic shield to the formation of zinc dendrites.[41] In-terms of energy storage, the dual cations and anions of the hybrid electrolyte further initiate reversible adsorption–desorption and intercalation processes on the Gr–C cathode side, resulting in

This journal is © The Royal Society of Chemistry 2022

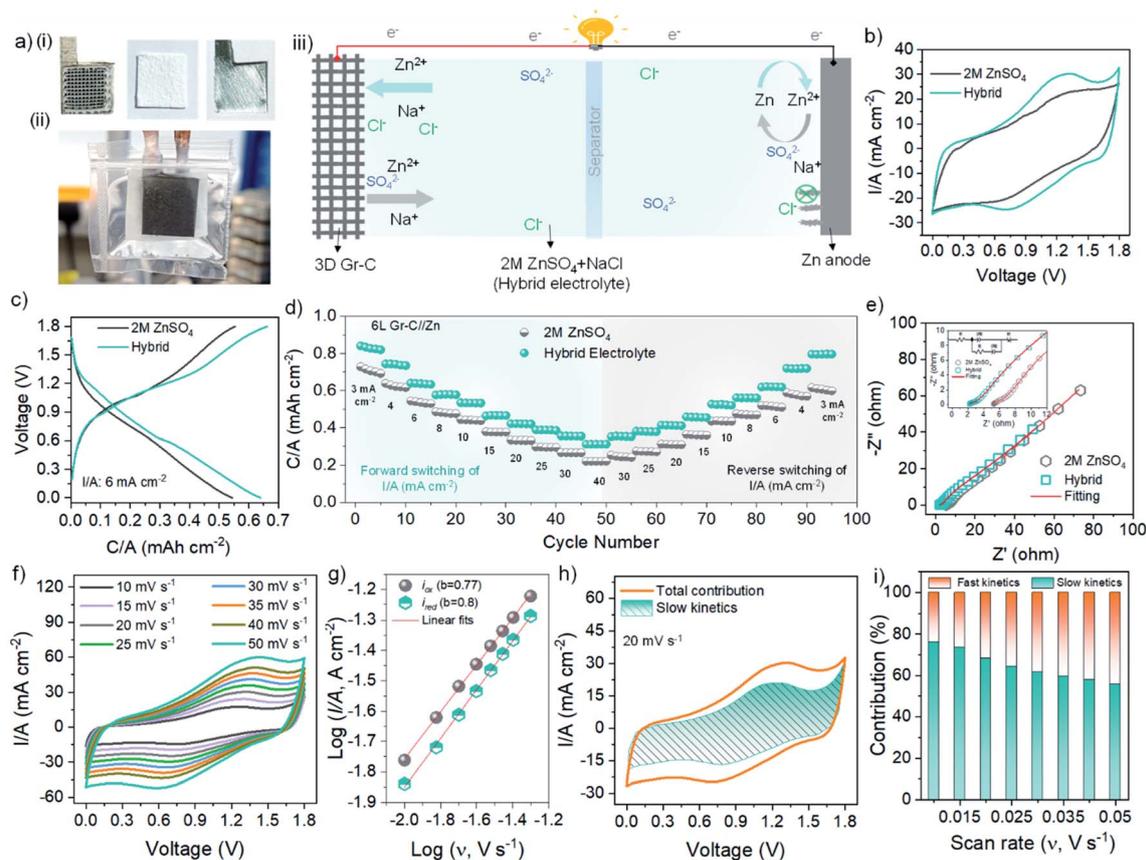*J. Mater. Chem. A*, 2022, **10**, 15665–15676 | **15669**

Fig. 3 Electrochemical properties of ZHCs full cells using 3D printed Gr−C composite as cathode, polished Zn metal as anode and glassy fiber paper as separator with the two-different electrolytes. (a) Photographs of (i) cell components, (ii) Gr−C//Zn pouch cell and (iii) schematic illustration of 3D printed Gr−C//Zn filled with hybrid electrolyte. Comparative (b) CV and (c) charge−discharge curves of 6L Gr−C//Zn cells measured at a constant scan rate of 20 mV s$^{-1}$ and $I/A$ of 6 mA cm$^{-2}$ using pristine ZnSO$_4$ and hybrid electrolyte respectively. Comparative (d) charge−discharge rate performance of Gr−C//Zn cells under forward and reverse switching $I/A$'s of 3−40 mA cm$^{-2}$ and (e) Nyquist plots of 6L Gr−C//Zn cells, demonstrating improved energy storage properties with hybrid electrolyte-based ZHC. (f) CV curves of hybrid electrolyte-based 6L Gr−C//Zn cell analysed at various scan rates of 10−50 mV s$^{-1}$ and (g) $b$-values obtained using the peak $I/A$'s collected from the corresponding CV curves. (h) CV curves of 6L Gr−C//Zn cell obtained at 20 mV s$^{-1}$, illustrating mixed capacitive current from the fast-kinetic processes (aroused by the adsorption/desorption of Na$^+$ and Zn$^{2+}$ cations) and diffusion-controlled current from the slow-kinetic processes (surface oxidation/reduction of Gr−C with anions). (i) Histograms of capacitive- and diffusion-controlled contributions measured at different scan rates.

high-capacity and rate capability.[42,43] Moreover, the use of the hybrid electrolyte accompanied the disappearance of undesirable side products on the surface of 3D Gr−C cathode, maintaining its high conductivity throughout the energy storage process, as confirmed by the *ex situ* characterisation of 3D Gr−C (Fig. S9†). As detailed in Fig. 3b and c, the hybrid electrolyte-based ZHC demonstrates better capacitive/redox behaviour, improved capacity, and high-rate capability compared with the pristine ZnSO$_4$ electrolyte-based ZHC. Using the hybrid electrolyte in comparison with pristine ZnSO$_4$, the electrochemical properties of 3D Gr−C//Zn cell were examined. When the ZHC cells were cycled within the voltage range of 0−1.8 V, the hybrid-electrolyte ZHC showed a pair of redox humps at ∼1.25 V and ∼0.75 V, as shown in the comparative CV plot of Fig. 3b. The faradaic behaviour of the ZHC could be attributed to the reversible ion oxidation and reduction on the surface of the carbon cathode and to the zinc faradaic reactions on the anode of the 3D Gr−C; while the capacitive-behaviour of 3D Gr−C is

ascribed to the adsorption/desorption of Na$^+$ and Zn$^{2+}$ cations on the cathode.[44] The estimated ratio of diffusion- and capacitive-behaviour of ZHC is shown in the following discussion. From the comparative CV plot, it is also evident that the current response and CV integral area of the hybrid electrolyte are higher than that of the pristine electrolyte cell, suggesting high electrochemical energy storage. The capacity of 3D electrodes was evaluated using galvanostatic charge−discharge (GCD) analysis. The comparison of GCD curves in Fig. 3c also reveals that the hybrid electrolyte ZHC has a high areal capacity ($C/A$) of 0.64 mA h cm$^{-2}$ at a current density ($I/A$) of 6 mA cm$^{-2}$, superior to the 0.54 mA h cm$^{-2}$ capacity for the pristine electrolyte cell. To gain insight about the effect of Na$^+$ ions on the energy storage performance, a ZHC device was also fabricated using a 2 M NaCl electrolyte (without any ZnSO$_4$). The CV and GCD curves of the device showed that Na$^+$ cations are actively involved in the energy storage process, especially in the voltage region of 3D Gr−C cathode (Fig. S15†). However, the areal

15670 | *J. Mater. Chem. A*, 2022, 10, 15665–15676

This journal is © The Royal Society of Chemistry 2022

capacity ($C/A$: 0.16 mA h cm$^{-2}$ at 6 mA cm$^{-2}$) of the pristine NaCl electrolyte cell is poor compared with the pristine ZnSO$_4$ and the hybrid electrolyte that we proposed. The relatively lower performance of pristine NaCl cell could be due to the deficiency of the Zn$^{2+}$ ions plating/stripping process on the Zn anode side. These results indicate that the inclusion of NaCl in ZnSO$_4$ not only suppresses the dendrites on the Zn anode side, but it also demonstrates improved energy storage performance. The difference in electrochemical performance between the pristine and hybrid electrolytes was further investigated using GCD rate measurements at different current densities. As it can be seen in Fig. 3d, the hybrid electrolyte leads to an increased capacity ($C/A$: 0.84 mA h cm$^{-2}$ at 3 mA cm$^{-2}$) and rate capability (37.2% at high $I/A$ of 40 mA cm$^{-2}$) as compared to the use of pristine ZnSO$_4$ ($C/A$: 0.72 mA h cm$^{-2}$ at 3 mA cm$^{-2}$ with rate capability of 30.3% at 40 mA cm$^{-2}$). The Nyquist plots in Fig. 3e further corroborates the higher ionic conductivity and lower resistance of the hybrid electrolyte ZHC, as well as reduced charge transfer resistance when compared to the pristine ZnSO$_4$ electrolyte (Fig. S8†). The electrochemical kinetics and reversibility of 3D Gr–C//Zn hybrid electrolyte cells were also analysed via cyclic voltammetry at various scanning speeds, ranging from 10 to 50 mV s$^{-1}$ (Fig. 3f). As shown in Fig. 3f, the CV integral area gradually increases upon increasing the scan rate. In addition, the anodic and cathodic current peaks only present a small shift towards forward and reverse potentials with increasing scan rate, which suggests a quasi-reversible electrochemical processes between hybrid ions and 3D Gr–C. The electro-chemical kinetic of Gr–C//Zn cell can be further quantified using the power law $i = a\nu^b$, where $i$ is the peak current ($I/A$), $\nu$ is scan rate (V s$^{-1}$) and $a$ and $b$ are adjustable parameters.[45] The charge-storage mechanism is diffusion-controlled (slow kinetic) when the $b$ value is close to 0.5, whereas it is controlled by capacitive processes (fast kinetic) when the $b$ value is close to 1. The corresponding $b$ values for the anodic and cathodic peaks of 6L Gr–C//Zn cell were calculated with a linear fitting of log $i_{ox}$ and $i_{red}$ vs. log $\nu$, resulting in $b$ values of 0.77 and 0.8 (Fig. 3g) for the anodic and cathodic peaks respectively. This reveals the simultaneous contribution of capacitive and diffusion-controlled behaviours to the charge storage in the hybrid elec-trolyte Gr–C//Zn cell. Evidently, the kinetic results also corrob-orate that both anions and cations of the hybrid electrolyte are responsible for the mixed charge storage process in the device. The modified power law ($i = S_1\nu + S_2\nu^{1/2}$) is then applied to obtain the ratio of capacitive ($S_1\nu$) vs. diffusion-controlled ($S_2\nu^{1/2}$) contributions in the total capacity of the Gr–C//Zn hybrid electrolytic cell.[46,47] At a scanning rate of 20 mV s$^{-1}$, capacitive- and diffusion-controlled contributions were calculated to be 31.8% and 68.2% of the total capacity in Gr–C//Zn cell (Fig. 3h). The corresponding contributions at different scan rates were also quantified and included in the histogram of Fig. 4i.

The effect of the mass loading/number of printed layers of the Gr–C cathode on the electrochemical performance was also analysed in hybrid electrolyte devices (Fig. 4a). As presented in Fig. 4a(i), the charge–discharge areal capacities ($C/A$) increased upon increasing the number of printed layers from 3 to 12 and the areal mass loading ($M/A$) from 12.5 to 52 mg cm$^{-2}$. The low

capacity of the 3L electrode can be attributed to the lower mass loading and mechanical stability of thinner electrodes, that can easily result in lower accessibility of electrolyte ions and restricted electron transport inside the electrode structure. The initial-cycle coulombic efficiency (CE) of the corresponding cells in Fig. S14a† reveals that the 8-layer Gr–C//Zn device has the highest CE of 95% compared with the other cells. Although the $C/A$ increases with mass loading up to the 8L Gr–C//Zn cell (Fig. 4a(ii)), the rise in $C/A$ between the 8–12L cell is modest (1.08 mA h cm$^{-2}$ vs. 1.12 mA h cm$^{-2}$ at $I/A$ of 3 mA cm$^{-2}$). When the gravimetric capacities ($C/M$) at different $I/A$ are compared, the 6L Gr–C//Zn cell demonstrates higher capacity than the 8L cell, while the 12L Gr–C//Zn cell shows much lower $C/M$ (Fig. 4a(iv)). This behaviour could be ascribed to the hindrance of increased charge transport along with the sluggish diffusion of the electrolyte ions into the thick multi-layered 3D Gr–C cathodes. Increased internal voltage (iR) (Fig. S14b†) could also be the reason for the lower charge storage capability of the 12L Gr–C//Zn at increasing current densities, compared with the other layers. The interconnected composite architecture of the 8L-cathodes along with its optimized porosity and high conductivity, provides rapid paths for quick penetration of the electrolyte ions and shorten the ion diffusion paths to store high $C/A$. Therefore, the 8L electrode shows the highest areal performance, which is crucial for application in portable devices where the available footprint area is limited. It is also worth mentioning that the 8L Gr–C//Zn cell showed much higher $C/A$ than the previously reported 3D printed Zn-ion capacitors, as presented in Fig. S16d.† The higher energy storage of 3D printed Gr–C structures in comparison with thin-film Gr–C-based ZHC cells were also included in Fig. S10.† Further comparisons on electrochemical performance (effect of printing layers) and volumetric capacity (mA h cm$^{-3}$) of the 3D Gr–C//Zn cells using pristine ZnSO$_4$ versus hybrid electrolyte are reported in Fig. S11–S16.† The energy and power densities are important parameters to determine the practical applicability of energy storage devices. The calculated areal energy density ($E_d/A$) and power density ($P_d/A$) of 3–12L Gr–C//Zn cells were included in the Ragone plot in Fig. 4b. Considering the $C/A$ and rate capability, the 8L Gr–C//Zn cell showed a maximum $E_d/A$ of 0.87 mW h cm$^{-2}$ at a $P_d/A$ of 2.67 mW cm$^{-2}$, and it retains an $E_d/A$ of 0.42 mW h cm$^{-2}$ at a high $P_d/A$ of 31.72 mW cm$^{-2}$. Owing to their high energy density and power density, the ZHC pouch cells could easily light up a light-emitting diode (Fig. S17†), demonstrating the practical potential of the 3D Gr–C//Zn cells. Remarkably, the obtained energy storage properties of our hybrid electrolyte 3D Gr–C//Zn cells are one to three orders of magnitude higher (Fig. 4b) than the previously reported 3D printed microsupercapacitors and Zn-ion capacitors, based on activated carbon (AC), reduced graphene oxide (rGO), printed MXenes and CNTs (Table S2†). To demonstrate the effectiveness of our hybrid electrolyte in controlling the dendrite formation and stable capacity, GCD cycling was performed on Gr–C//Zn cells. Fig. 4c shows the long-term cycling durability of the hybrid electrolyte Gr–C//Zn cells (from 3 to 12L), together with the pristine electrolyte Gr–C//Zn cell (6L). Although the carbon-based cathodes have high stability during the cycling process,

This journal is © The Royal Society of Chemistry 2022

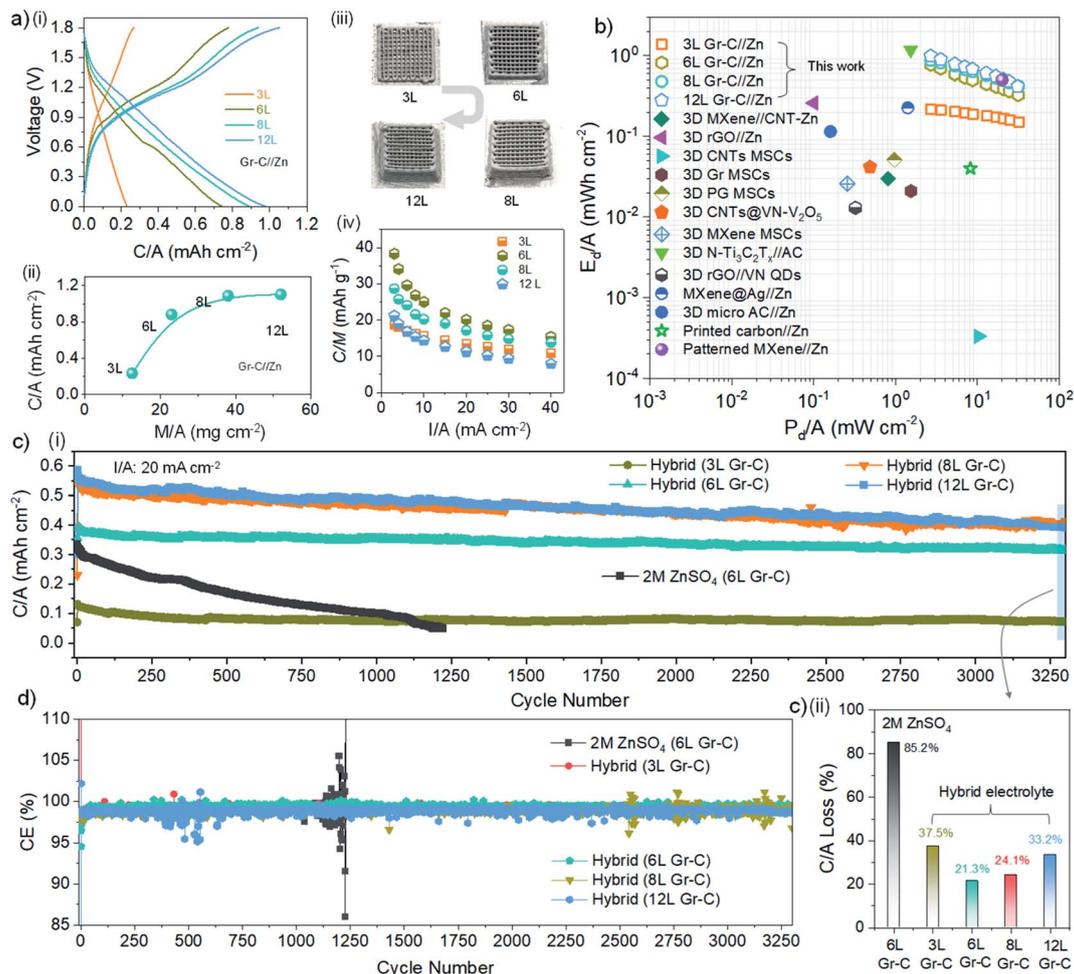J. Mater. Chem. A, 2022, **10**, 15665–15676 | **15671**

Fig. 4 Electrochemical properties of 3D Gr–C//Zn cells in hybrid electrolyte with different 3D cathodes. (a) (i) charge–discharge capacities of multi-layer (3–12L) 3D printed Gr–C//Zn full cells measured at a current density of 3 mA cm$^{-2}$ with the hybrid electrolyte (top left), (ii) areal capacity (bottom left) of 3–12L Gr–C//Zn cells with various $M/A$, (iii) photographic images of 3–12L cathodes (top right), which inherently provide different mass loadings of Gr–C composites and (iv) gravimetric capacities (bottom right) 3–12L Gr–C//Zn cells with different charge–discharge $I/A$. (b) Ragone plot showing benchmark areal energy density of hybrid electrolyte-based 3D Gr–C//Zn cell plotted as a function of power density, which were compared with previously reported 3D printed ZHCs and 3D microsupercapacitors. (c) Comparative long-term cycling stability and (d) coulombic efficiency of 3D printed Gr–C//Zn cells using pristine ZnSO$_4$ electrolyte and hybrid electrolytes.

undesirable side products and rapid growth of dendrites on the Zn anode gradually suppress the durability of Zn-ion cells with pristine ZnSO$_4$. At a high charge–discharge rate $I/A$ of 20 mA cm$^{-2}$, the 6L Gr–C//Zn cell assembled with the pristine ZnSO$_4$ electrolyte demonstrates decreased capacity upon extended GCD cycles and failed its operation after 1220 cycles with a capacity loss of 85.2%. This could be ascribed to the rapid growth of insulating products on the surface of the Zn anode (Fig. 2e) and layered formation of zinc sulphate hydrate and zinc oxide species on cathode (JCPDS card # 010-4031 and 080-4983), as detailed in *ex situ* XRD analysis (Fig. S9†). The gradually piled-up dendrites on the Zn anode can penetrate through the separator and cause short-circuits to fail the ZHC operation, as demonstrated by the unstable CE behaviour in the pristine electrolyte (Fig. 4d). On the contrary, the Gr–C//Zn cells tested with hybrid electrolyte initiates uniform plating/stripping of Zn$^{2+}$ ions on the Zn anode and protects its surface, thus leading

to an extended life cycle. After 3300 cycles at 20 mA cm$^{-2}$, the capacity loss for the high-mass loaded 3–12L Gr–C//Zn cells in hybrid electrolyte were about 37.5%, 21.3%, 24.1% and 33.2% with the CE of 99.2%, 99.6%, 98.9% and 98.7%, respectively. These results suggest a better capacity retention of hybrid electrolyte-based Gr–C//Zn cells compared with conventional ZnSO$_4$ electrolyte.

Alongside cycling durability and energy density benchmarks, monitoring the rate performance of energy storage devices is also important as it determines the device applicability in high-power advanced applications. Conventional processes to determine the rate performance of metal-ion batteries and electrochemical capacitors include galvanostatic charge–discharge (GCD) analysis at various current densities ($I/A$). Especially, acquiring rate performance of high-mass loaded 3D ZHC at low $I/A$ using the GCD method is very slow and time consuming (Fig. S18† and 5a). For example, using the charge–

15672 | *J. Mater. Chem. A*, 2022, **10**, 15665–15676

This journal is © The Royal Society of Chemistry 2022

discharge current $I/A$ of 0.2 mA cm$^{-2}$, the time taken for a single GCD cycle of 12L Gr–C//Zn cell is ~15 h, as presented in Fig. S18h.† Although, the GCD rate performance is faster at high rates, the device experiences severe voltage drops (Fig. 3g(ii)) and undesirable side products on the anode surface. Therefore, the rapid determination of the rate performance is advantageous, especially for variable mass loadings ($M/A$) of multiple electrodes and their devices. Recently, Heubner et al., and Tian et al., proposed a straightforward and rapid chronoamperometric (CA) method to measure the capacity-rate measurements of LIB electrodes, ranging from extremely high to low rates.[48,49] Moreover, CA can be used to produce several hundreds of data points. Considering the merits of CA measurement and the lack of rate studies on metal-ion capacitors, we believe that this technique is a great tool to measure the rate performance of ZHCs in a short period. Therefore, here we employed CA tests to assess the rate performance of high-mass loading 3D Gr–C//Zn-based HSCs for the first time. In Fig. 5b the CA data of 3D Gr–C//Zn cell are reported and represent the transient decay of $I/A$ with respect to the discharge time. As shown in the CA data of the 3D Gr–C//Zn cell, the $I/A$ response over time suggests that the high $I/A$ of 350–2.5 mA cm$^{-2}$ can be rapidly measured within 36 s. Upon increasing the discharge time, the recorded $I/A$ transients of 3D Gr–C//Zn cell declines to the extremely low currents of 0.34 and 0.1 mA cm$^{-2}$ after 360 and 3600 s, indicating the effectiveness of this method for fast counting of $I/A$ and time transients. On the contrary, up to 11 h (depending on the $M/A$ of

3D electrodes) are required to measure the rate performance using conventional GCD tests at a charge–discharge $I/A$ of 3–40 mA cm$^{-2}$, as presented in Fig. 5a and S18b–g.† The rate ($R$, h$^{-1}$) can be quantified using the GCD and CA methods with the following equations:[50,51]

$$R_{GCD} = \frac{I/A}{C/A} \tag{1}$$

$$R_{CA} = \frac{I/A}{\int_0^t I/A \, dt} \tag{2}$$

where, $I/A$ is the current density and $C/A$ is the areal capacity calculated by GCD and $\int_0^t I/A \, dt$ is the areal capacity ($C/A$) quantified using CA plot. In eqn (1), the $R_{GCD}$ is related to the actual charge/discharge time at specific $I/A$. For $R_{CA}$, capacity-rate data points can be obtained by integrating the current at a specific time. To test the $R_{CA}$ using CA method, we have employed various 3D printed (from 3 to 12L) Gr–C//Zn cells with pristine ZnSO$_4$ and hybrid electrolytes. For each 3D Gr–C//Zn cell, we measured the CA and applied eqn (2) to obtain the $C/A$ and $R$ data, as shown in Fig. 5c–f. Compared with conventional GCD (open symbols in Fig. 5c–f), this CA method can quickly provide rate data with increased density of data sets. In addition, $C/A$–$R$ plots show good agreement between CA and GCD measurements up to 8L Gr–C//Zn cells. However, there is a slight variation between the CA and GCD capacities on 12L Gr–C//Zn cell, which might be ascribed either to the ion-
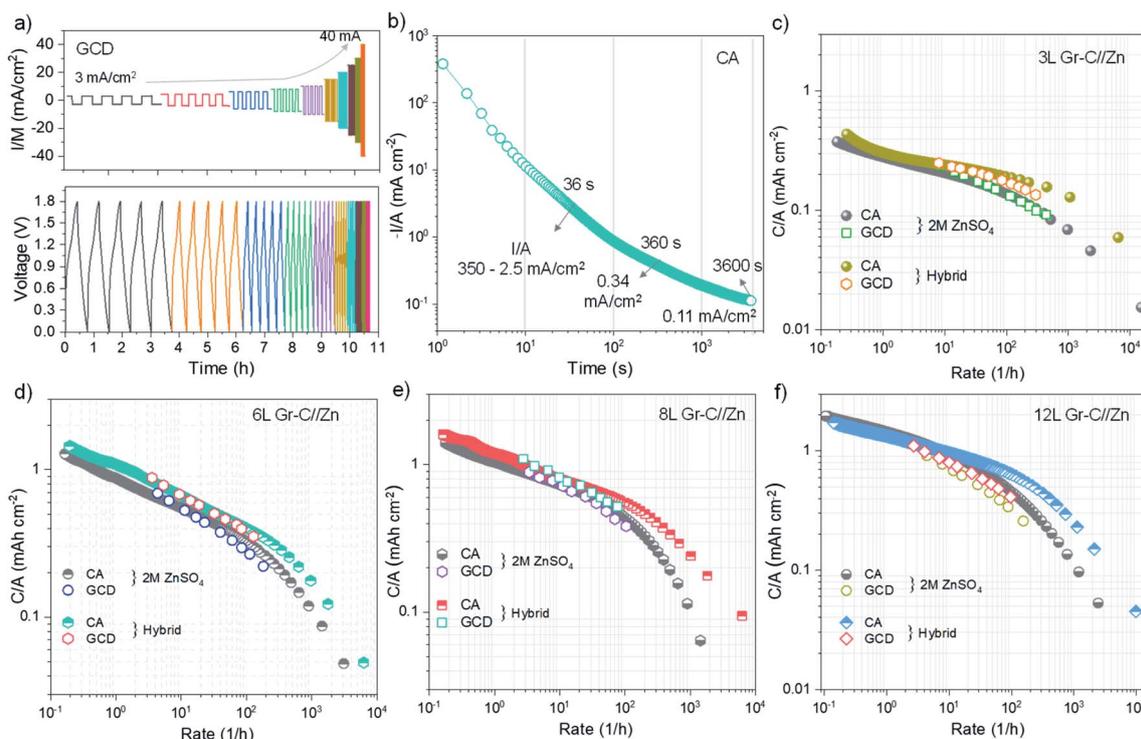


**Fig. 5** Comparison of capacity-rate data using conventional GCD and CA method. (a) Rate measurements of 3D Gr–C//Zn cell analysed using conventional GCD tests (bottom) with increasing charge–discharge $I/A$ of 3 to 40 mA cm$^{-2}$ (top). (b) $I/A$ transient as a function of time obtained via the CA method for 12L 3D Gr–C//Zn cell. (c–f) comparison of capacity vs. rate curves obtained via CA and GCD methods using 3–12L printed Gr–C//Zn cells in pristine ZnSO$_4$ and hybrid electrolytes.

penetration on extremely thick Gr–C or to the poor adhesion of the active material. From the $R^{-1}$ plots of Fig. 5c–f, it is also noticeable a constant capacity ($C/A$) displayed at low rate which then falls at higher rate. The decreased $C/A$ could be attributed to the fact that the high $I/A$ region of the CA data is associated with fast rates (Fig. 5b), therefore electrolyte ions do not have sufficient time to initiate the slow-kinetic transport within the thick 3D Gr–C electrode. This means that the major contributions to the $I/A$ transient are electronic, and that the diffusion contribution to the $I/A$ transient is small. From the $R$-plots we can infer that the hybrid electrolyte ZHCs also show large capacities upon increasing the number of Gr–C layers, which are higher than the pristine electrolyte cell. Considering the fast rate performance of 3D Gr–C//Zn cells, the CA method could be considered as an alternative and reliable procedure to measure the capacity-rate data for high-mass loading energy storage devices. Overall, the proposed cost-effective NaCl additive in $ZnSO_4$ electrolyte tackle the Zn anode dendrite formation and in conjunction with the high-mass loaded 3D cathodes enable the increase of the capacity towards highly durable ZHC.

## 3. Conclusion

In conclusion, we reported high-performance ZHCs using a 3D printed Gr–C composite structure as cathode and a Zn foil as anode with low-cost NaCl additive in $ZnSO_4$ (hybrid) electrolyte. This approach resulted in a controlled plating/stripping of Zn, improved areal capacity, and enhanced cycling stability. The hybrid electrolyte provides two key beneficial features on the anode and cathode, which are: a dynamic electrostatic shield layer and a pH regulating effect which reduces the irreversible side reactions and dendrites formation. In addition, the high surface area and the good electrical conductivity of the 3D printed 8L Gr–C cathode enable a dual-ion electrochemical mechanism, which leads to greater areal capacity of 0.84 mA h cm$^{-2}$ at 3 mA cm$^{-2}$ and longer cycling stability of 78.7% at 20 mA cm$^{-2}$ compared with pristine electrolyte ZHCs. Through printing layers optimization (3–12L), the hybrid electrolyte-based 3D Gr–C//Zn cell provides high areal energy and power densities (0.87 mW h cm$^{-2}$ and 31.7 mW cm$^{-2}$), which are superior to the state-of-the-art of 3D printed electrochemical devices. Furthermore, the rate performance of the highly mass loaded 3D cathodes in ZHC cells were also evaluated using a rapid CA method, which is an advantageous alternative to the time consuming conventional GCD methods. This work demonstrates a pathway towards the cost-effective development of efficient electrolytes and highly conductive 3D electrodes with high-capacity energy storage devices.

## 4. Experimental details

### 4.1. Materials

Two-dimensional graphene (Gr) platelets (5 μm lateral size, surface area 120–150 m$^2$ g$^{-1}$, Sigma-Aldrich), aqueous SWCNTs dispersion (C, Tuball™, OCSiAl), carbon nanotubes powder (CNTs, Sigma-Aldrich), sodium carboxymethyl cellulose (CMC, ~250 000 $M_w$, Sigma-Aldrich), zinc sulphate heptahydrate

($ZnSO_4 \cdot 7H_2O$, Sigma-Aldrich), sodium chloride (NaCl, Sigma-Aldrich), polished Zn metal foil (Zn, 0.2 mm thick, Puratronic®, 99.9%, Alfa Aesar), Copper foil (Cu, Sigma-Aldrich) and graphite foil (0.4 mm thick, Alfa Aesar) were commercially obtained. Deionized (DI) water with a resistivity: ~18.0 MΩ cm$^{-1}$ was used throughout the experiments. All the chemicals were of analytical grade and used as received without further purification.

### 4.2. Preparation and characterisation of graphene–carbon nanotube (Gr–C) inks

The aqueous ink based on Gr–C heterostructures was prepared using modified procedure of our earlier work.[52] Briefly, 1.4 g of Gr platelets and 0.34 g of CMC powder were added to a high density polyethelene plastic jar containing water dispersed SWCNTs (0.4 wt%, 4 mg ml$^{-1}$). The mixture was then homogenized using a high-speed planetary mixer (Thinky ARE-250) at 2000 rpm for 5 min. The printable Gr–C ink was then stored in the fridge and re-homogenized before being used. For comparison of conductivity and rheological properties, the aqueous Gr ink (without SWCNTs dispersion) was also prepared using the same portion of Gr platelets and CMC with DI-water. For structural comparison, the Gr–C ink was also prepared using similar procedure with CNTs powder (5%), Gr platelets (95%) and CMC binder in DI water (Fig. S3†). The rheological properties of the prepared inks were examined with a rotational rheometer (HR1-TA Instruments) using 40 mm stainless steel parallel plates at 25 °C. For all measurements, the distance between the two plates was adjusted to 1000 μm and a solvent trap was also placed to minimize the water evaporation of the inks.

### 4.3. Direct-ink writing of 3D printed Gr–C heterostructure

For printing, the homogenized Gr–C ink was transferred into a 3 mL plastic syringe using a plastic spatula. The ink loaded syringe with a 410 μm diameter nozzle was then fixed to a displacement-controlled plunger, which provides a continuous pressure supply. A robocaster – 3D printer with three reconfigurable heads was used for the extrusion-based DIW of aqueous Gr–C inks. Woodpile-shaped 3D microstructures (3–12 layers) were printed on graphite foil using a printing speed of 6 mm s$^{-1}$. After drying at room temperature, the printed Gr–C electrodes were stabilized *via* thermal sintering (at 350 °C for 30 min) under argon gas flow (Ar, ~0.5 mbar). Thermal gravimetric analysis/differential thermal analysis (SCINCO, TGA N-1000/1500) was used to demonstrate the effective removal of inactive components from the 3D Gr–C electrodes.

### 4.4. Material characterisation

The microstructures of the Gr–C and cycled Zn anodes were analysed using scanning electron microscopy (SEM, Zeiss Auriga) and transmission electron microscopy (TEM, JEOL JEM-200CX) images. The XRD patterns were collected on an X-ray diffractometer (Bruker D2 Phaser diffractometer) with Cu Kα radiation ($\lambda$ = 1.5406 Å). Raman spectra of the printed and cycled electrodes were tested by a Raman spectrometer

15674 | *J. Mater. Chem. A*, 2022, **10**, 15665–15676

This journal is © The Royal Society of Chemistry 2022

(Renishaw inVia Qontor confocal Raman microscope) using a 532 nm laser with a laser power of 0.5 mW. XPS analysis on the annealed Gr–C was collected on a X-ray photoelectron spectrometer (Thermo Scientific K-Alpha$^+$), equipped with a microfocused Al Kα X-ray source. The measurements were performed at room temperature using a 20 eV energy pass with the energy step of 0.1 eV. The XPS data were fitted using Voigt functions using the Avantage software package. The electrical conductivity of Gr–C and Gr thin-films (coated on glass substrate) was measured *via* I–V curves using a Gamry Interface 1000 system.

### 4.5. Electrolyte preparation

The hybrid electrolyte was prepared by mixing the 2 M ZnSO$_4$ and 2 M NaCl salts in DI water at room temperature. The mixtures were then placed on a magnetic plate under vigorous stirring to ensure complete dissolution of the mixed salts. The pristine electrolyte was also prepared with 2 M ZnSO$_4$ in DI water for comparison. The pH and ionic conductivity of the corresponding electrolytes were recorded using portable pH metre (Hanna instruments Checker™) and a two-electrode system (RS-12 digital multimetre).

### 4.6. Fabrication and electrochemical characterizations

Pouch-type Zn//Zn, Zn//Cu and 3D Gr–C//Zn cells were assembled using pristine 2 M ZnSO$_4$ and hybrid electrolytes with glassy fiber membrane (Whatman GF/A with a thickness of 260 μm, Sigma-Aldrich) as a separator. The electrochemical properties of the pouch cells were studied using a multichannel VMP-3 workstation (Bio-Logic Science Instruments). Chronopotentiometry (CP) and *in situ* electrochemical impedance spectroscopy (EIS) were employed for metal-ion plating/stripping of pristine and hybrid electrolyte Zn//Zn symmetric cells. Energy storage performance of full cells based on 3D Gr–C//Zn cells (with pristine and hybrid electrolytes) were analysed using cyclic voltammetry (CV), galvanostatic charge–discharge (GCD), chronoamperometry (CA) rate performance and long-term cycling performance. The EIS measurements of full cells were performed using a voltage sine wave of 10 mV amplitude across a frequency range of 100 kHz to 0.01 Hz. *Ex situ* mapping images as well as depth profiles of cycled Zn foils (100 × 100 μm$^2$) with pristine ZnSO$_4$ and hybrid electrolytes were analysed using Time-of-Flight Secondary Ion Mass Spectrometry (ToF-SIMS V system, ION-TOF GmbH) with a 25 keV Bi$^+$ primary ion beam.

## Conflicts of interest

There are no conflicts to declare.

## Acknowledgements

## References

1 Y. Liang, C.-Z. Zhao, H. Yuan, Y. Chen, W. Zhang, J.-Q. Huang, D. Yu, Y. Liu, M.-M. Titirici, Y.-L. Chueh, H. Yu and Q. Zhang, *InfoMat*, 2019, **1**, 6–32.

2 Y. Lyu, X. Wu, K. Wang, Z. Feng, T. Cheng, Y. Liu, M. Wang, R. Chen, L. Xu, J. Zhou, Y. Lu and B. Guo, *Adv. Energy Mater.*, 2021, **11**, 2000982.

3 J. Xie and Y.-C. Lu, *Nat. Commun.*, 2020, **11**, 2499.

4 A. Manthiram, *ACS Cent. Sci.*, 2017, **3**, 1063–1069.

5 V. Etacheri, R. Marom, R. Elazari, G. Salitra and D. Aurbach, *Energy Environ. Sci.*, 2011, **4**, 3243–3262.

6 L. Dong, W. Yang, W. Yang, Y. Li, W. Wu and G. Wang, *J. Mater. Chem. A*, 2019, **7**, 13810–13832.

7 G. Pistioa, *Battery Operated Devices and Systems*, 2009, pp. 1–15.

8 X. Liu, Y. Sun, Y. Tong, X. Wang, J. Zheng, Y. Wu, H. Li, L. Niu and Y. Hou, *Nano Energy*, 2021, **86**, 106070.

9 J. Yin, W. Zhang, N. A. Alhebshi, N. Salah and H. N. Alshareef, *Adv. Energy Mater.*, 2021, **11**, 2100201.

10 H. Tang, J. Yao and Y. Zhu, *Adv. Energy Mater.*, 2021, **11**, 2003994.

11 M. Monev, L. Mirkova, I. Krastev, H. Tsvetkova, S. Rashkov and W. Richtering, *J. Appl. Electrochem.*, 1998, **28**, 1107–1112.

12 C. Li, X. Xie, S. Liang and J. Zhou, *Energy Environ. Mater.*, 2020, **3**, 146–159.

13 T. Wang, C. Li, X. Xie, B. Lu, Z. He, S. Liang and J. Zhou, *ACS Nano*, 2020, **14**, 16321–16347.

14 L. Ma, Q. Li, Y. Ying, F. Ma, S. Chen, Y. Li, H. Huang and C. Zhi, *Adv. Mater.*, 2021, **33**, 2007406.

15 L. E. Blanc, D. Kundu and L. F. Nazar, *Joule*, 2020, **4**, 771–799.

16 Z. Kang, C. Wu, L. Dong, W. Liu, J. Mou, J. Zhang, Z. Chang, B. Jiang, G. Wang, F. Kang and C. Xu, *ACS Sustainable Chem. Eng.*, 2019, **7**, 3364–3371.

17 Y. Zeng, X. Zhang, R. Qin, X. Liu, P. Fang, D. Zheng, Y. Tong and X. Lu, *Adv. Mater.*, 2019, **31**, 1903675.

18 J. F. Parker, C. N. Chervin, E. S. Nelson, D. R. Rolison and J. W. Long, *Energy Environ. Sci.*, 2014, **7**, 1117–1124.

19 Y. Du, Y. Li, B. Bin Xu, T. X. Liu, X. Liu, F. Ma, X. Gu and C. Lai, *Small*, 2021, 2104640.

20 W. Guo, Y. Zhang, X. Tong, X. Wang, L. Zhang, X. Xia and J. Tu, *Mater. Today Energy*, 2021, **20**, 100675.

21 M. Cui, Y. Xiao, L. Kang, W. Du, Y. Gao, X. Sun, Y. Zhou, X. Li, H. Li, F. Jiang and C. Zhi, *ACS Appl. Energy Mater.*, 2019, **2**, 6490–6496.

22 X. Guo, Z. Zhang, J. Li, N. Luo, G.-L. Chai, T. S. Miller, F. Lai, P. Shearing, D. J. L. Brett, D. Han, Z. Weng, G. He and I. P. Parkin, *ACS Energy Lett.*, 2021, **6**, 395–403.

23 K. A. Owusu, X. Pan, R. Yu, L. Qu, Z. Liu, Z. Wang, M. Tahir, W. A. Haider, L. Zhou and L. Mai, *Mater. Today Energy*, 2020, **18**, 100529.

This journal is © The Royal Society of Chemistry 2022

J. Mater. Chem. A, 2022, **10**, 15665–15676 | **15675**

24 Z. Zhou, X. Zhou, M. Zhang, S. Mu, Q. Liu and Y. Tang, *Small*, 2020, **16**, 2003174.

25 Y.-G. Lee and G.-H. An, *ACS Appl. Mater. Interfaces*, 2020, **12**, 41342–41349.

26 Y. Shao, Z. Sun, Z. Tian, S. Li, G. Wu, M. Wang, X. Tong, F. Shen, Z. Xia, V. Tung, J. Sun and Y. Shao, *Adv. Funct. Mater.*, 2021, **31**, 2007843.

27 T. Xin, Y. Wang, N. Wang, Y. Zhao, H. Li, Z. Zhang and J. Liu, *J. Mater. Chem. A*, 2019, **7**, 23076–23083.

28 Z. Fan, J. Jin, C. Li, J. Cai, C. Wei, Y. Shao, G. Zou and J. Sun, *ACS Nano*, 2021, **15**, 3098–3107.

29 J. Wu, X. Zhang, Z. Ju, L. Wang, Z. Hui, K. Mayilvahanan, K. J. Takeuchi, A. C. Marschilok, A. C. West, E. S. Takeuchi and G. Yu, *Adv. Mater.*, 2021, **33**, 2101275.

30 S. Tagliaferri, A. Panagiotopoulos and C. Mattevi, *Mater. Adv.*, 2021, **2**, 540–563.

31 M. Peng, D. Shi, Y. Sun, J. Cheng, B. Zhao, Y. Xie, J. Zhang, W. Guo, Z. Jia, Z. Liang and L. Jiang, *Adv. Mater.*, 2020, **1908201**, 1–8.

32 J. C. Mareque-Rivas, R. Prabaharan and R. T. Martín de Rosales, *Chem. Commun.*, 2004, 76–77.

33 B. Gavriel, N. Shpigel, F. Malchik, G. Bergman, M. Turgeman, M. D. Levi and D. Aurbach, *Energy Storage Mater.*, 2021, **38**, 535–541.

34 X. Ji, *eScience*, 2021, **1**(2), 99–107.

35 M. Mouanga, P. Berçot and J. Y. Rauch, *Corros. Sci.*, 2010, **52**, 3984–3992.

36 L. M. Baugh, *Electrochim. Acta*, 1979, **24**, 657–667.

37 L. Wang, W. Wu, W. Sun, Z. Yang, S. Wang and G. Liu, *Chem. Eng. J.*, 2019, **373**, 8–22.

38 J. Y. Song, H. H. Lee, Y. Y. Wang and C. C. Wan, *J. Power Sources*, 2002, **111**, 255–267.

39 L. Ma, M. A. Schroeder, T. P. Pollard, O. Borodin, M. S. Ding, R. Sun, L. Cao, J. Ho, D. R. Baker, C. Wang and K. Xu, *Energy Environ. Mater.*, 2020, **3**, 516–521.

40 F. Ding, W. Xu, G. L. Graff, J. Zhang, M. L. Sushko, X. Chen, Y. Shao, M. H. Engelhard, Z. Nie, J. Xiao, X. Liu, P. V Sushko, J. Liu and J.-G. Zhang, *J. Am. Chem. Soc.*, 2013, **135**, 4450–4456.

41 F. Ding, W. Xu, G. L. Graff, J. Zhang, M. L. Sushko, X. Chen, Y. Shao, M. H. Engelhard, Z. Nie, J. Xiao, X. Liu, P. V Sushko, J. Liu and J.-G. Zhang, *J. Am. Chem. Soc.*, 2013, **135**, 4450–4456.

42 C. Yang, J. Chen, X. Ji, T. P. Pollard, X. Lü, C.-J. Sun, S. Hou, Q. Liu, C. Liu, T. Qing, Y. Wang, O. Borodin, Y. Ren, K. Xu and C. Wang, *Nature*, 2019, **569**, 245–250.

43 I. A. Rodríguez-Pérez, L. Zhang, J. M. Wrogemann, D. M. Driscoll, M. L. Sushko, K. S. Han, J. L. Fulton, M. H. Engelhard, M. Balasubramanian, V. V. Viswanathan, V. Murugesan, X. Li, D. Reed, V. Sprenkle, M. Winter and T. Placke, *Adv. Energy Mater.*, 2020, **10**, 2001256.

44 J. Yin, W. Zhang, W. Wang, N. A. Alhebshi, N. Salah and H. N. Alshareef, *Adv. Energy Mater.*, 2020, **10**, 2001705.

45 T. S. Mathis, N. Kurra, X. Wang, D. Pinto, P. Simon and Y. Gogotsi, *Adv. Energy Mater.*, 2019, **9**, 1902007.

46 G. Nagaraju, S. C. Sekhar, B. Ramulu and J. S. Yu, *Energy Storage Mater.*, 2021, **35**, 750–760.

47 B. Yao, H. Peng, H. Zhang, J. Kang, C. Zhu, G. Delgado, D. Byrne, S. Faulkner, M. Freyman, X. Lu, M. A. Worsley, J. Q. Lu and Y. Li, *Nano Lett.*, 2021, **21**, 3731–3737.

48 R. Tian, P. J. King, J. Coelho, S.-H. Park, D. V Horvath, V. Nicolosi, C. O'Dwyer and J. N. Coleman, *J. Power Sources*, 2020, **468**, 228220.

49 C. Heubner, C. Lämmel, A. Nickol, T. Liebmann, M. Schneider and A. Michaelis, *J. Power Sources*, 2018, **397**, 11–15.

50 S.-H. Park, R. Tian, J. Coelho, V. Nicolosi and J. N. Coleman, *Adv. Energy Mater.*, 2019, **9**, 1901359.

51 R. Tian, P. J. King, J. Coelho, S.-H. Park, D. V Horvath, V. Nicolosi, C. O'Dwyer and J. N. Coleman, *J. Power Sources*, 2020, **468**, 228220.

52 S. Tagliaferri, G. Nagaraju, A. Panagiotopoulos, M. Och, G. Cheng, F. Iacoviello and C. Mattevi, *ACS Nano*, 2021, **15**, 15342–15353.

**15676** | *J. Mater. Chem. A*, 2022, **10**, 15665–15676

This journal is © The Royal Society of Chemistry 2022